remote sensing

MDPI

Article

A Multi-Frequency SAR Framework for Methane Emission Estimation in Thai Rice Paddies

Nuntikorn Kitratporn [1,*], Kanjana Koedkurang [1], Panu Nueangjamnong [1], Kittiphop Simachokchai [1], Chompunut Chayawat [1], Shinichi Sobue [2] and Thuy Le Toan [3,4]

[1] Geo-Informatics and Space Technology Development Agency (Public Organization), Bangkok 10210, Thailand
[2] Japan Aerospace Exploration Agency (JAXA), Tsukuba 305-8505, Japan
[3] GlobEO, 18 Avenue Edouard Belin, 31400 Toulouse, France
[4] Centre d'Etudes Spatiales de la Biosphère, 31400 Toulouse, France
* Correspondence: nuntikorn.kit@gistda.or.th

Highlights

What are the main findings?

- An SAR-based framework integrating Sentinel-1 phenology detection (planting and harvest MAE of 6.1 and 8.3 days; 97.0% detection rate) and ALOS-2 water-level classification (per-stage Balanced Accuracy 0.59–0.89).
- End-to-end CH_4 estimation achieves a full-pipeline MAE of 21.4% relative to ground-based calculations. Component-wise error analysis identifies water-regime classification as the dominant uncertainty source, while the IPCC Tier 1 emission factor structural range (−32% to +48%) exceeds all algorithmic errors combined.

What are the implications of the main findings?

- The framework demonstrates the potential for a scalable, spatially explicit approach to national MRV systems, offering a high-resolution alternative to conventional aggregate statistics.
- The findings underscore L-band SAR's potential sensitivity to sub-canopy inundation, which can support the remote verification of climate-smart practices, such as Alternate Wetting and Drying.

Abstract

Rice cultivation is a major source of methane (CH_4) emission in the agricultural sector, with a significantly higher global warming potential than carbon dioxide. Accurate and scalable quantification of CH_4 from rice paddies is essential for carbon accounting. This study presents an automated framework for estimating rice CH_4 emissions from irrigated paddies in the central plain of Thailand, integrating multi-sensor Synthetic Aperture Radar (SAR) observations with the IPCC methodology. The framework combines Sentinel-1 C-band SAR time series for phenological detection, ALOS-2 PALSAR-2 L-band full-polarimetric SAR for water regime classification, and IPCC water-scaling factors corresponding to Continuous Flooding, Single Drainage, or Multiple Drainage regimes. Evaluated across five stratified holdout sets, the phenology detection algorithm achieved planting and harvesting date Mean Absolute Errors of 6.1 ± 1.4 and 8.3 ± 1.7 days, with a 97.0% ± 2.7% operational detection rate. Water regime classification employed rice growth stage-specific Support Vector Machine classifiers with Radial Basis Function kernels (SVM-RBF), achieving per-stage test Balanced Accuracy ranging from 0.59 to 0.89. End-to-end integration using a four-track counterfactual decomposition yielded a full-pipeline mean absolute error of 18.5 ± 4.5 kg CH_4 ha^{-1} (21.4% of the mean ground-based CH_4 calculation) and a mean bias of 3.5 ± 5.8 kg CH_4 ha^{-1}. Water level classification was confirmed as the dominant

Check for updates

Academic Editor: Guido D'Urso

Received: 26 April 2026
Revised: 15 June 2026
Accepted: 30 June 2026
Published: 4 July 2026

Copyright: © 2026 by the authors. Licensee MDPI, Basel, Switzerland. This article is an open access article distributed under the terms and conditions of the Creative Commons Attribution (CC BY) license.

algorithmic uncertainty source, while the IPCC Tier 1 emission factor structural range (−32% to +48% of the default) exceeded all algorithmic errors combined. The proposed framework provides a spatially explicit approach for integrating multi-frequency SAR data into IPCC-compliant methane estimation, supporting Monitoring, Reporting, and Verification applications.

Keywords: GHG; Sentinel-1; ALOS-2 PALSAR-2; IPCC; MRV; food security

1. Introduction

Agricultural activities are one of the largest anthropogenic sources of methane (CH_4), a potent greenhouse gas with a global warming potential approximately 27–30 times greater than carbon dioxide (CO_2) over a 100-year horizon [1]. Among agricultural systems, flooded rice paddies contribute approximately 8–12% of total global anthropogenic CH_4 [2,3], driven by methanogenesis under anaerobic soil conditions. Southeast Asia dominates global rice production, accounting for more than two-thirds of the world's harvested paddy area [4]. In Thailand, rice ecosystems underpin national food security while also contributing substantially to the national greenhouse gas (GHG) inventory in the agricultural sector [5].

Accurate quantification of methane emissions from rice cultivation is essential for national carbon accounting and mitigation strategies. Direct chamber-based measurements are accurate at the plot scale but are labor-intensive and spatially limited, hindering their integration into regional Monitoring, Reporting, and Verification (MRV) systems [6]. Following the Intergovernmental Panel on Climate Change (IPCC) guidelines, methane emissions are estimated as the product of activity data, a baseline emission factor (EF), and scaling factors (SFs) that account for water management, organic amendments, and cultivation conditions [7].

Currently, Thailand's national reporting estimates CH_4 emissions using activity data from harvested areas categorized by rice ecosystem, paired with emission factors differentiated by region [5]. However, this ecosystem-based approach does not yet account for the significant mitigation potential of field-level water management. Effective mitigation relies on practices such as Alternate Wetting and Drying (AWD), which reduces methane emissions without compromising grain yields [8]. Such water management interventions are applicable mainly in irrigated rice systems, where water inputs are actively controlled by farmers [8]. Rainfed, deepwater, and upland rice ecosystems depend on rainfall or topographic inundation and do not offer equivalent leverage for emission reduction [7]. Although incorporating field-level water management is a priority for future inventories [5], capturing its spatial heterogeneity at the landscape scale requires a scalable remote sensing approach. Satellite-based Earth Observation (EO) provides such a scalable solution. In tropical regions with persistent cloud cover, Synthetic Aperture Radar (SAR) outperforms optical sensors due to its all-weather imaging capability and sensitivity to surface water and vegetation structure [9].

Prior EO-based studies have demonstrated CH_4 estimation capabilities at multiple scales. At global scale, Chen et al. [3] mapped monthly rice paddy inundation using Landsat time series, estimating global rice CH_4 at 39.3 ± 4.7 Tg yr^{-1} and placing Thailand among the five largest emitting countries. At continental scale, Ouyang et al. [10] combined eddy covariance measurements with optical satellite predictors in a machine learning model to produce gridded CH_4 flux maps across Monsoon Asia. At regional scale, satellite-based inverse modeling using TROPOMI atmospheric CH_4 observations has been applied to constrain rice emissions in China [11], and data-driven Gradient Boosting approaches

using meteorological and satellite-derived indices have demonstrated high-resolution CH_4 mapping in paddy fields [12]. At the field scale, SAR-based studies have most directly targeted IPCC-compatible CH_4 estimation.

Previous studies also utilized SAR observations. Torbick et al. [13] integrated multi-scale satellite data with biogeochemical models to map greenhouse gas emissions in the Red River Delta, Vietnam. In the Mekong Delta, Arai et al. [14] combined ALOS-2 PALSAR-2 inundation maps with IPCC Tier 1 factors, demonstrating that L-band SAR effectively detects sub-canopy flooding. More recently, a multi-sensor SAR approach within an IPCC framework was applied to paddy fields in West Java, Indonesia [15]. These studies confirm the technical feasibility of integrating SAR observations into the IPCC emission estimation framework.

Effective integration of SAR observations into an end-to-end CH_4 framework requires combining two complementary SAR frequencies. C-band SAR (5.6 cm wavelength) time-series data can detect rice phenology, including planting and harvesting dates, which define the temporal window for methane production [16–19]. Its short wavelength is highly sensitive to canopy structural changes at field establishment, but backscatter sensitivity declines as the rice canopy closes, limiting its utility for sub-canopy water detection during the main growing season [9,20]. L-band SAR (23.5 cm wavelength) provides deeper canopy penetration, reaching the soil-water surface beneath a closed rice canopy where C-band energy is attenuated [20,21]. However, the longer L-band revisit interval may miss brief phenological events such as the field establishment backscatter minimum. The two SAR frequencies, therefore, serve complementary roles that neither band can fulfill alone, and accurate estimation of plot-level CH_4 activity data requires combining C-band phenology detection with L-band sub-canopy inundation classification.

Despite these demonstrations, significant gaps remain. Existing studies integrating SAR-derived inputs with the IPCC Tier 1 framework [14,15] have involved experimental plots within a single growing season. Per-plot water management classification in these studies is often substituted by uniform assumptions, masking the landscape and seasonal variability that drives field-level CH_4 differences. The full end-to-end pipeline has, therefore, not been validated against independent field records across multiple seasons and diverse water management practices. A further unresolved issue concerns error attribution. No study has decomposed the contributions of phenology detection error and water regime classification error to end-to-end CH_4 uncertainty, nor compared these algorithmic errors against the IPCC Tier 1 emission factor structural range. Without this attribution, practitioners cannot identify where improvement effort yields the greatest return.

This study addresses both gaps by developing and evaluating an automated SAR-based framework for estimating irrigated rice CH_4 emission density in the Central Plain of Thailand. The specific objectives are to (1) detect planting and harvesting dates using time-series C-band SAR data; (2) classify water management regimes during the cultivation period using L-band SAR observations; and (3) estimate CH_4 emissions by coupling SAR-derived parameters with IPCC emission factors and water-regime-specific scaling factors. Results are reported as emission density ($kgCH_4\ ha^{-1}$), enabling direct comparison between fixed monitoring networks and probabilistic survey designs independently of plot area.

2. Materials and Methods

2.1. Overview

The proposed framework is shown in Figure 1, which integrates three sequential processing pipelines. The first pipeline processes the Sentinel-1 VH time-series to detect planting and harvesting dates, yielding the growing season duration. The second pipeline classifies each ALOS-2 PALSAR-2 acquisition within the Sentinel-1-detected season window

as either Inundated or Non-inundated using a machine learning approach, then assigns a water-scaling factor based on the proportion of Non-inundated observations. The last pipeline combines both outputs with the IPCC CH_4 emission formula:

$$CH_4\ (\text{kg season}^{-1}) = A \times D \times EF \times SF_w \quad (1)$$

where A (ha) is cultivated areas, D (days) is growing season duration, EF ($kgCH_4\ ha^{-1}\ day^{-1}$) is the IPCC Tier 1 default emission factor for Southeast Asia at 1.22 with a structural range of 0.83–1.81 (−32% to +48% of the default), and SF_w (unitless) is a water management scaling factor which represents three water regimes including Continuously Flooded, Single Drainage, and Multiple Drainage [7]. As the objective is to evaluate remote sensing components in isolation from area measurements, plot-level area data are not incorporated. Results are reported as emission density ($kgCH_4\ ha^{-1}\ season^{-1}$) to enable direct comparison between ground-based calculations and satellite-derived estimation.

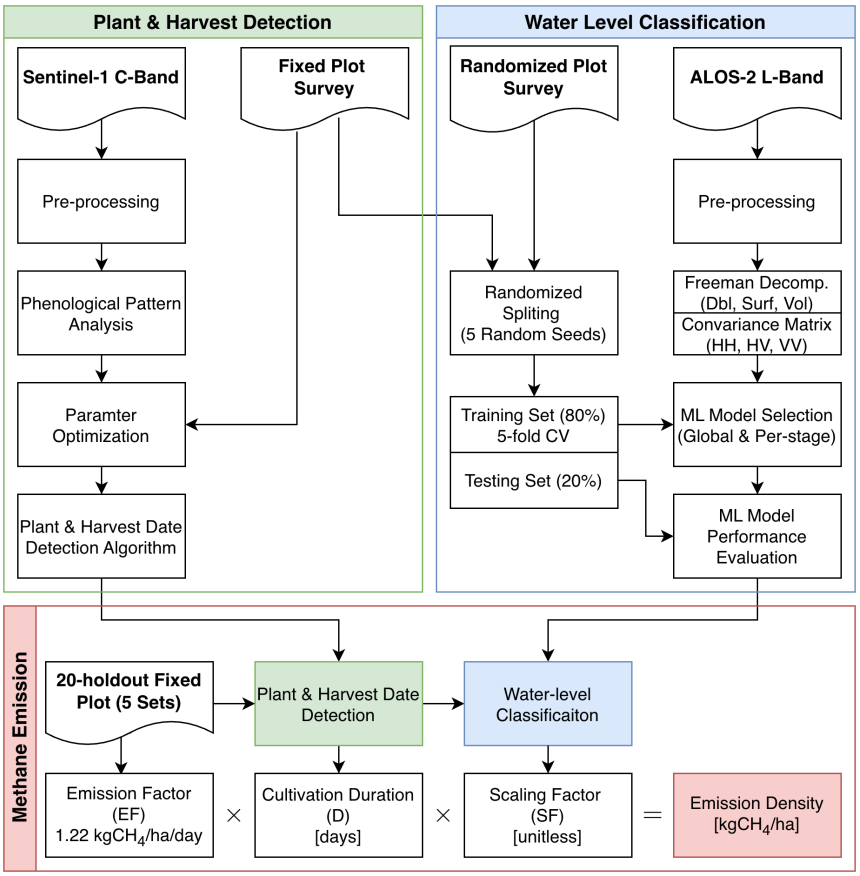


Figure 1. Overview of the SAR-based rice CH_4 emission estimation framework, integrating Sentinel-1 phenology detection, ALOS-2 water level classification, and IPCC emission estimation.

In terms of the IPCC Tier framework, this study is classified as Tier 1 applied with per-plot SAR-derived activity data. While baseline EF and SF values are taken from IPCC defaults [7], the use of satellite observations to derive plot-specific activity data improves spatial resolution and temporal specificity over conventional national-inventory statistics. The key distinction from a conventional Tier-1 application is that activity data are derived per-plot from satellite observations rather than from aggregated national statistics. Elevation to Tier 2 would require replacing the default EF with locally measured, country-specific values derived from direct chamber flux measurements [5,22].

2.2. Study Area

Figure 2 shows the study area in Thailand's lower central plains with extensive irrigated paddy fields. The area covers four provinces, which include Suphan Buri, Ang Thong, Sing Buri, and Chainat. This region lies within the Chao Phraya river basin and supports one of the most intensively cultivated rice landscapes in the country with both single and double cropping systems. Ground surveys were conducted across fixed monitoring plots. An additional set of randomized ground survey plots was conducted to collect water-level management and rice growing stages.

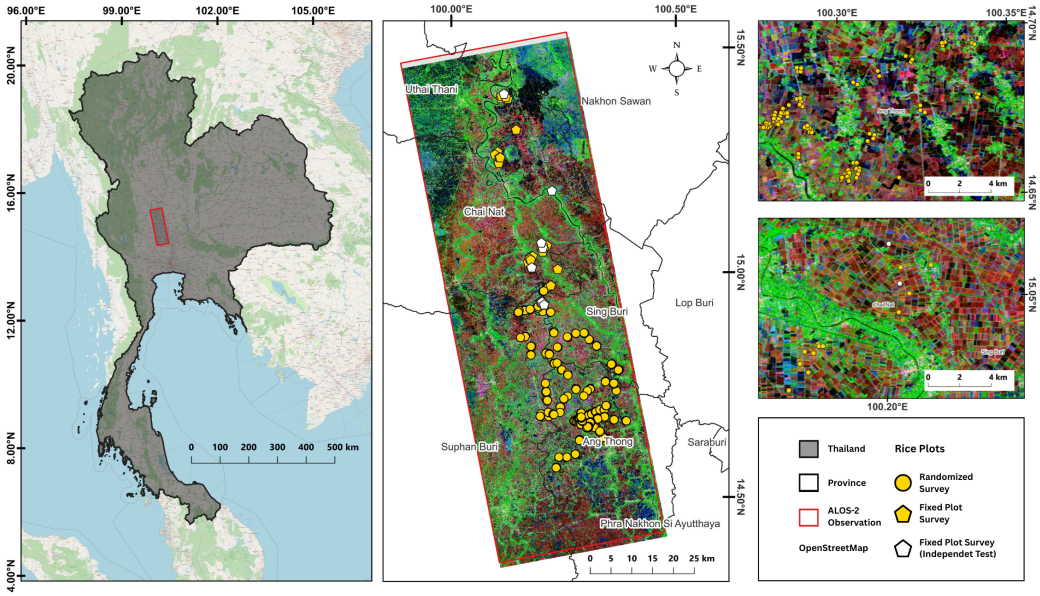


Figure 2. Study area in Thailand's central plain across Suphan Buri, Ang Thong, Sing Buri, and Chainat provinces, showing ground survey plots within the ALOS-2 satellite observation path.

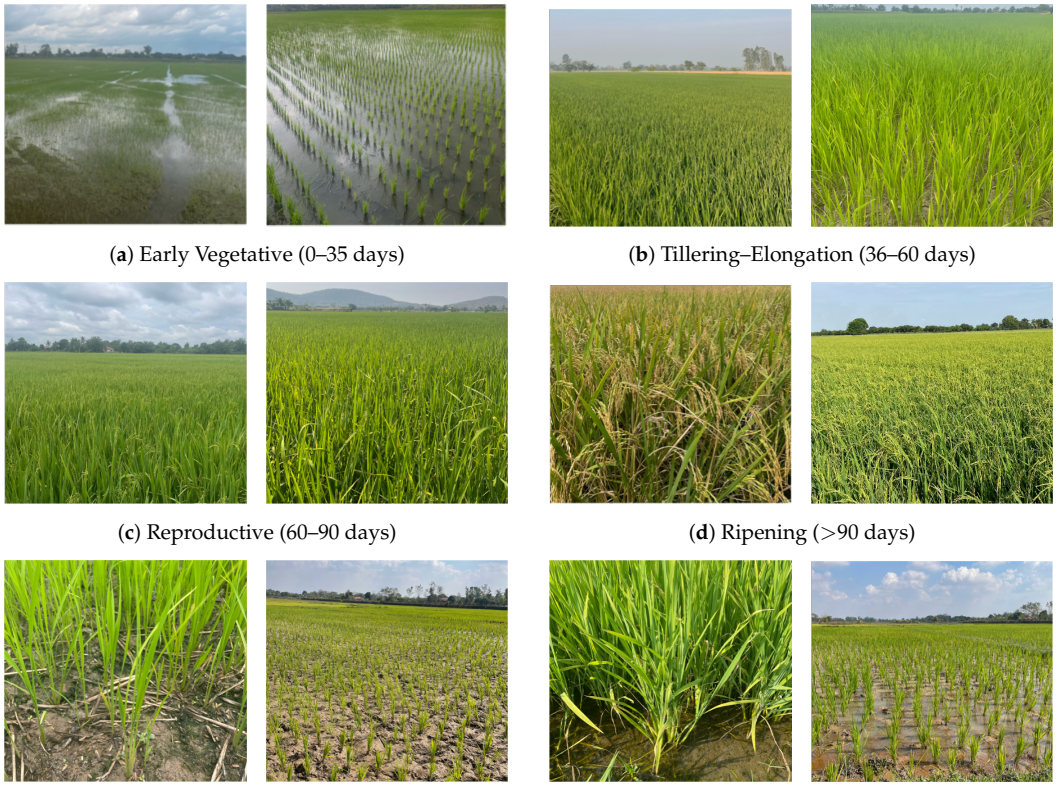
2.3. Ground Survey

Ground data were collected using two survey methods. All surveys were conducted within one day in coordination with ALOS-2 acquisition schedules to ensure close coincidence between satellite and field observations. The ground surveys recorded the actual in-situ water level state. The rice growth stage was recorded using a standardized four-stage phenological classification scheme along with water level category, including Inundated and Non-inundated, as shown in Figure 3.

Sixty fixed monitoring plots were established across the study area, with 20 plots per growing season. Three growing seasons were covered, including Season 1 (June–October 2024), Season 2 (November 2024–March 2025), and Season 3 (April–August 2025). Each fixed plot was equipped with three manual water-level monitoring instruments which were used by trained field surveyors to record inundation depth. Precise planting and harvesting dates were also recorded. An additional set of plots was surveyed using a randomized design. This survey was introduced to broaden spatial and agronomic coverage, particularly to augment underrepresented water management classes. A total of 399 unique samples were collected during June–September 2025. The exact planting and harvesting dates were not captured.

To obtain robust performance estimates, the 60 fixed plots were partitioned into five stratified sets using a repeated random assignment strategy. In each set, 20 plots (33% of fixed plot samples) were withheld as holdout and the remaining 40 served as the training pool for all parameter optimization and model development. Holdout sets were stratified to maintain approximate proportions of Season 1, Season 2, and Season 3 plots across

sets. This approach preserves representation of water management classes including the Continuously Flooded plots concentrated in Seasons 1 and 3. The manual survey observations were not subject to holdout exclusion as they lack planting and harvesting dates and cannot contribute to end-to-end evaluation.



(**a**) Early Vegetative (0–35 days) (**b**) Tillering–Elongation (36–60 days)

(**c**) Reproductive (60–90 days) (**d**) Ripening (>90 days)

(**e**) Non-inundated (≤ 0 cm) (**f**) Inundated (>0 cm)

Figure 3. Photographic examples of ground-truth rice phenological stages and field water-level conditions. Stages (**a**–**d**) illustrate canopy progression, while (**e**,**f**) contrast the baseline water levels.

2.4. Satellite Data

2.4.1. Sentinel-1 C-Band

Sentinel-1 C-band SAR imagery was obtained from the Google Earth Engine (GEE) cloud-computing platform [23] as Level-1 Ground Range Detection (GRD) products. Data were acquired in descending passes at a nominal 12-day repeat cycle, covering all 60 fixed plots from April 2024 to December 2025. Only the VH backscatter time series was used due to its greater sensitivity to rice canopy volume scattering and exhibiting the characteristic temporal pattern which can be used to identify rice cultivation phenology [9,16,18,20,24]. VV backscatter retains a stronger surface-scattering contribution throughout the growing season and does not exhibit the same sharp, consistent minimum at field establishment. VH backscatter coefficients were converted to linear scale for zonal averaging per plot and subsequently reconverted to decibels (dB) for algorithm application. Technical specifications for both Sentinel-1, including frequency, spatial resolution, polarisation, revisit time, and acquisition coverage, are summarised in Table S1.

2.4.2. ALOS-2 L-Band

ALOS-2 carries the Phased Array type L-band Synthetic Aperture Radar-2 (PALSAR-2) operating at a center frequency of 1.2 GHz with a 14-day nominal revisit cycle. The longer L-band wavelength enables canopy penetration more effectively than C-band, which provides sensitivity to sub-canopy water conditions that are attenuated by the rice plant volume [21,25]. The full-polarimetric PALSAR-2 data were acquired in Stripmap mode

at 6 m spatial resolution. Level 1.1 product in the CEOS format was processed using the Sentinel Application Platform (SNAP) provided by ESA [26]. The processing steps included radiometric calibration, Lee sigma speckle filtering, and terrain correction using SRTM 1 sec DEM. Freeman–Durden decomposition [27] was applied to get surface scattering (surf), volume scattering (vol), and double-bounce (dbl). Additionally, the covariance matrix (C_3) was also applied to extract VV, HV, and HH polarization. This yields a total of six input features. Pixel values were extracted using a two-pixel interior buffer to reduce backscatter contamination from plot-boundary features including irrigation channels, vegetated bunds, and adjacent non-rice land cover. Such features can generate anomalous returns including double-bounce scattering between the water surface and raised bund walls. A one-pixel buffer is insufficient to clear narrow bunds, while a larger buffer would reduce the effective sampling area of smaller plots to an impractical size. Technical specifications for ALOS-2 PALSAR-2, including frequency, spatial resolution, polarisation, revisit time, and acquisition coverage, are summarised in Table S1.

2.5. Framework Development

2.5.1. Rice Phenology Detection

The algorithm was developed through systematic analysis of Sentinel-1 VH backscatter temporal profiles from fixed plots, covering growing seasons of 105–133 days. Inspection of these profiles revealed a characteristic VH pattern tied to rice age (Figure 4). VH decreases sharply from field establishment, reaching a minimum at approximately 10–15 days when the inundated or waterlogged surface dominates the radar response while the young, sparse canopy contributes minimally to backscatter. This is followed by a recovery as canopy biomass accumulates through the tillering and reproductive phases, reflecting increasing volume scattering from elongating stems and leaves.

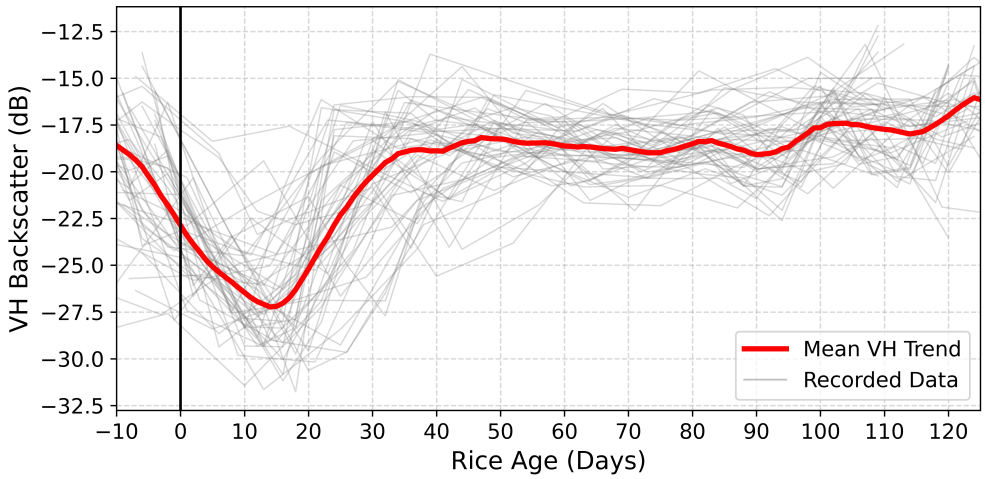


Figure 4. Sentinel-1 VH backscatter temporal profiles aligned to days after planting (DAP) for all 60 monitoring plots (grey) with the mean trend (red).

The identified transitions form the physical basis for the planting detection algorithm, which operates through three sequential steps. First, the algorithm scans the VH time-series for a local minimum below a specified valley threshold (`valley_thresh`). When such a minimum is found, the planting date is assigned to the prior Sentinel-1 observation, since the VH minimum occurs 10–15 days after field establishment. Second, a false-alarm reset cancels the candidate if VH recovers sharply above a recovery threshold (`recover_thresh`) within a specified window (`false_alarm_days`). This rejects short-duration inundation events such as pre-season land preparation flooding that produces a spurious early minimum before actual field establishment. Third, a refinement step searches within a subsequent window

(`refine_days`) and updates the planting candidate if any of the following conditions are met: (i) a subsequent, lower valley is detected; (ii) the depth difference between the two valleys falls within a defined tolerance; or (iii) only one signal within the window passes the valley threshold. This handles the case where pre-season land preparation flooding produces a spurious early VH minimum, followed by the true planting event weeks later.

Following planting date detection, harvest is identified as the first occurrence of VH recovering above a minimal threshold (`harvest_min_vh`) set in either a peak ($VH_{t-1} \leq VH_t \geq VH_{t+1}$) or ascending ($VH_{t-1} \leq VH_t \leq VH_{t+1}$) backscatter pattern. These patterns reflect the biological signal of crop maturation approaching harvest. If no qualifying pattern is detected after the harvesting search period (`window_thresh`) but before 132 days, the harvesting date is assigned based on the expected season duration.

Algorithm parameters were optimized by grid search across the six parameters listed in Table 1. For each holdout set, the grid search was applied to the 40 non-holdout training plots. The selection criterion required both planting and harvest to achieve $\geq$ 95% detection accuracy within $\pm$24-day error on the training pool where achievable; if no parameter combination met this threshold, the selection fell back to combinations achieving the maximum attainable detection rate. The objective was to minimize a composite error combining planting MAE and harvesting MAE, which are critical anchors for ALOS-2 stage alignment.

Table 1. Grid search parameter ranges for phenology detection. Grid search is applied independently to each of the five holdout sets using the 40 non-holdout training plots.

Parameter	Description	Search Range
valley_thresh	VH valley threshold for planting detection (dB)	−23.3, −22.7, −22.5, −22.3, −22.0, −21.7
recover_thresh	False-alarm cancellation VH threshold (dB)	−15.0, −14.7, −14.5, −14.3, −13.7, −13.0
false_alarm_days	False-alarm check window (days)	12, 24, 36, 48
refine_days	Valley refinement search window (days)	48, 60, 72, 84
harvest_min_vh	Harvest detection VH threshold (dB)	−18.0, −17.7, −17.5, −17.3, −17.0, −16.7
window_thresh	Lower bound of harvest search window (days)	95, 100, 105

Algorithm performance was evaluated under a unified protocol applied consistently across all five randomized sets. For each set, the algorithm was run on the full Sentinel-1 time-series of each plot without a pre-specified season window. When multiple candidate cycles were detected, the cycle whose planting date fell closest to the ground-truth planting date within a $\pm$60-day proximity window was selected. Plots for which no candidate fell within this window were recorded as missed detections and excluded from error metrics. Performance is reported as Mean Absolute Error (MAE), Root Mean Square Error (RMSE), Mean Bias Error (MBE), and the fraction of detections within $\pm$24 days of ground truth. These performance evaluations are computed for planting date, harvesting date, and growing season duration, where y_i denotes the ground-truth value and $\hat{y}_i$ is the detected value for plot i:

$$\text{MAE} = \frac{1}{n}\sum_{i=1}^{n}|y_i - \hat{y}_i| \tag{2}$$

$$\text{RMSE} = \sqrt{\frac{1}{n}\sum_{i=1}^{n}(y_i - \hat{y}_i)^2} \tag{3}$$

$$\text{MBE} = \frac{1}{n}\sum_{i=1}^{n}(\hat{y}_i - y_i) \tag{4}$$

2.5.2. Water Level Classification

The water level classification model was developed within the same five stratified datasets as used for the phenology detection algorithm. After excluding observations with missing values, the full usable dataset comprised 621–629 plot-stage observations from 439 rice plots. Table 2 summarizes the composition of the training pool per randomized set.

Table 2. Training pool composition per set based on five randomized set, excluding the 20-holdout fixed plot. Values that vary across the five sets are reported as mean (min–max).

Growth Stage	Total Obs.	Inundated		Non-Inundated	
		n	%	n	%
Early Vegetative	150 (147–152)	103 (101–106)	69	47 (45–50)	31
Tillering–Elongation	152 (150–153)	89 (86–91)	59	62 (61–65)	41
Reproductive	128 (127–130)	72 (69–74)	56	56 (54–59)	44
Ripening	196 (195–198)	82 (79–85)	42	114 (111–117)	58
Total	626 (621–629)	346 (340–352)	55	280 (276–284)	45

Eight classifiers were evaluated, which include Support Vector Machine with RBF kernel (SVM-RBF), Support Vector Machine (SVM-Linear), Logistic Regression, Random Forest, Gradient Boosting, XGBoost, AdaBoost, and Decision Tree. All models were evaluated using 5-fold stratified group cross-validation (CV) to prevent spatial data leakage between folds [28] and repeated across multiple random seeds. Classifier performance was estimated using 80%/20% splits of the training pool and reported as mean ± standard deviation. Class weights were set to account for class imbalance. Classification performance is reported using Balanced Accuracy (BA), F1 score, precision, and recall for the Non-inundated class, with true positive, true negative, false positive, and false negative represented by TP, TN, FP, and FN respectively. An aggregated confusion matrix summed across all five sets is also reported.

$$\text{Precision} = \frac{\text{TP}}{\text{TP} + \text{FP}} \tag{5}$$

$$\text{Recall} = \frac{\text{TP}}{\text{TP} + \text{FN}} \tag{6}$$

$$\text{F1} = \frac{2\,\text{TP}}{2\,\text{TP} + \text{FP} + \text{FN}} \tag{7}$$

$$\text{Balanced Accuracy (BA)} = \frac{1}{2}\left(\frac{\text{TP}}{\text{TP} + \text{FN}} + \frac{\text{TN}}{\text{TN} + \text{FP}}\right) \tag{8}$$

Six features derived from ALOS-2 full-polarimetric data were used without dimensionality reduction. Although the Freeman–Durden components (surf, vol, dbl) are mathematically derived from the C_3 covariance matrix (VV, HV, HH) and are, therefore, not statistically independent, the decomposition provides physically interpretable scattering contributions [27,29]. These six features carry discriminative information not easily separable in the raw intensity channels alone [30]. A global model was trained using all growth stages. Additionally, stage-specific models were independently trained for each of the four rice growth stages, including Early Vegetative, Tillering–Elongation, Reproductive, and Ripening. For each stage and randomized set, the per-stage model was selected only when its multi-seed cross-validation BA exceeded the global model's BA evaluated on the same stage subset. The final routing applied was determined by majority vote across the five sets. This routing criterion was applied using only the training pool, with no access to holdout data [28].

Feature importance was assessed using a model-independent approach. For each of the six features and four rice growth stages, a Mann–Whitney U test was performed to compare feature distributions between the Inundated and Non-inundated classes across the full combined dataset. The mean difference between classes ($\Delta\bar{x}$, Non-inundated minus Inundated) was used as the effect size, with larger absolute values indicating greater class discrimination. Statistical significance was assessed at $p < 0.05$ [31].

2.5.3. Methane Emission Estimation

The methane emission estimation integrates Sentinel-1 phenology detections and ALOS-2 water level classifications for the 20 holdout plots in each of the five stratified sets. Only ALOS-2 acquisitions whose dates fall within the Sentinel-1-detected growing season window are included in the SF assignment. For each plot and season, all ALOS-2 observations within the detected window are classified, and the count of Non-inundated predictions (n_{dry}) is used to assign the scaling factor according to the IPCC Tier 1 convention [7] (Table 3). Temporal continuity and observation intervals are not considered. Only the count of Non-inundated predictions within the detected window matters, consistent with IPCC Tier 1 protocol.

Table 3. Default CH_4 emission scaling factors for water regimes of irrigated rice during the cultivation periods relative to Continuously Flooded fields.

Water Regime	Trigger	Scaling Factor (SF)
Continuously Flooded	$n_{\text{dry}} = 0$	1.00
Single Drainage Period	$n_{\text{dry}} = 1$	0.71
Multiple Drainage Periods	$n_{\text{dry}} \geq 2$	0.55

To quantify the error contribution from each algorithmic component, a four-track evaluation was applied. The first track (ground-based baseline) estimates CH_4 using field-surveyed duration and recorded water level data, providing a reference against which all algorithmic errors are evaluated. The second track combines the SAR-based phenology detection algorithm with ground-truth water classification, isolating the error attributable to phenology detection alone. The third track retains ground-truth season duration while integrating the ML-based water regime classification, isolating the error attributable to water level classification alone. The fourth track applies the complete SAR-based pipeline, using both SAR-detected phenology and ML-based water classification to represent the fully operational system. Performance is reported as mean absolute error (MAE) and mean bias error (MBE) in kg CH_4 ha^{-1}, averaged across the 20 holdout plots and then across the five holdout sets.

3. Results

3.1. Rice Phenology Detection

The best-fit parameters were highly consistent across all five holdout experiments (Table 4). Four parameters, valley_thresh, recover_thresh, false_alarm_days, and refine_days, were identical in all five sets. The harvest detection parameters showed minor variation. The parameter harvest_min_vh ranged from −18.0 dB to −16.7 dB, while the parameter window_thresh was 105 days in four sets and 100 days in one. This consistency across independently drawn holdout partitions indicates that the optimized parameters are not sensitive to the specific assignment of plots to training or holdout groups.

Table 4. Modal optimal parameter values across five stratified holdout sets.

Parameter	Optimal Value	Unit
valley_thresh	−22.3	dB
recover_thresh	−15.0	dB
false_alarm_days	24	days
refine_days	84	days
harvest_min_vh	−17.3	dB
window_thresh	105	days

Across five stratified holdout sets, the phenology detection algorithm detected 97% ± 2.7% of plots per-set. The three missed detections occurred due to a pre-season land preparation flooding event that generated an early spurious VH minimum before actual sowing. For the successfully detected plots, the mean planting MAE was 6.1 ± 1.4 days, harvest MAE was 8.3 ± 1.7 days, and duration MAE was 8.2 ± 1.9 days. The fraction of detections within ±24 days was 96.9% ± 2.9% for planting, 98.9% ± 2.4% for harvest, and 98.9% ± 2.4% for duration. Figure 5 shows the signed error distribution per holdout set for all three outputs. Plant date errors were slightly positively biased (MBE = +2.6 days), while harvest and duration errors showed a consistent negative bias (harvest MBE = −1.8 days; duration MBE = −4.5 ± 1.1 days), reflecting the algorithm's tendency to detect slightly shorter growing seasons. All errors remained within the ±24-day threshold for the large majority of plot-season evaluations.

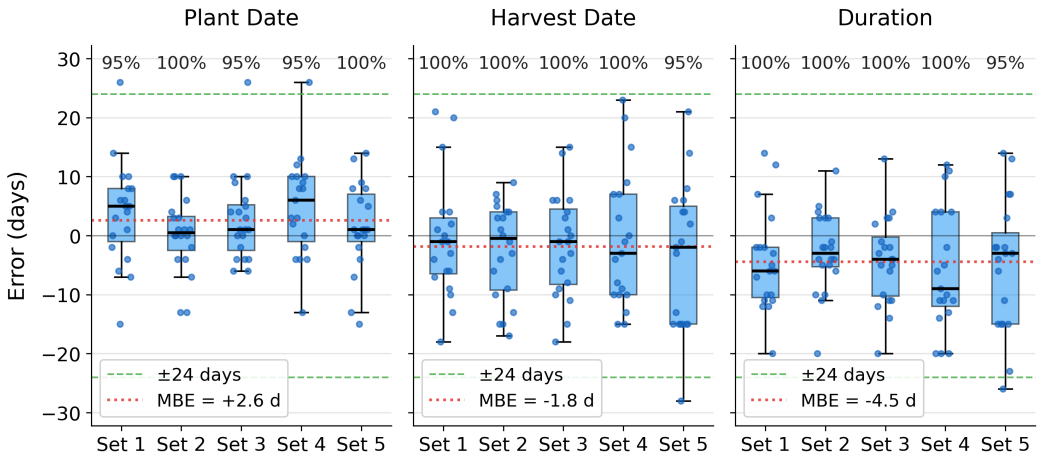


Figure 5. Error distribution across five stratified holdout sets for planting date, harvesting date, and season duration. Each box shows the median and interquartile range. Green dashed lines mark the ±24-day acceptable error threshold, while the red dotted line indicates the average Mean Bias Error (MBE).

3.2. Rice Water Regime Classification

SVM-RBF was the top-performing classifier across all five holdout sets. Classifier selection was based on cross-validation balanced accuracy (BA) computed on the training pool. Cross-validation was performed using five folds, with all observations from the same plot assigned to the same fold to prevent data leakage between training and validation subsets. The mean cross-validation BA was 0.68 ± 0.01 (range 0.664–0.688). Table 5 reports the full test-set performance, including balanced accuracy, F1 score, precision, and recall for both classes across all growth stages. The independently evaluated test BA on the held-out plots was 0.70 ± 0.01 (range 0.689–0.721).

Table 5. Water regime SVM-RBF classifier performance reported as mean ± SD across five stratified holdout sets. Overall metrics are averaged across all stages, while per-stage metrics are computed independently within each stage subset.

	Overall	Early Vegetative	Tillering–Elongation	Reproductive	Ripening
Balanced Accuracy	0.70 ± 0.01	0.89 ± 0.01	0.78 ± 0.02	0.59 ± 0.01	0.82 ± 0.03
Non-inundated (NI)					
F1	0.69 ± 0.01	0.72 ± 0.02	0.74 ± 0.03	0.57 ± 0.03	0.83 ± 0.04
Precision	0.68 ± 0.02	0.57 ± 0.02	0.76 ± 0.06	0.62 ± 0.03	0.81 ± 0.05
Recall	0.70 ± 0.01	1.00 ± 0.00	0.73 ± 0.04	0.53 ± 0.07	0.84 ± 0.06
Inundated (IN)					
F1	0.72 ± 0.01	0.87 ± 0.01	0.81 ± 0.01	0.60 ± 0.02	0.81 ± 0.03
Precision	0.73 ± 0.01	1.00 ± 0.00	0.80 ± 0.03	0.56 ± 0.04	0.83 ± 0.06
Recall	0.70 ± 0.02	0.77 ± 0.02	0.83 ± 0.04	0.65 ± 0.05	0.79 ± 0.05

Figure 6a shows the training-based routing signal, determined by cross-validation on training data only with no access to the holdout test set. The per-stage model was selected at Early Vegetative (BA 0.82 ± 0.02 vs. global BA 0.78 ± 0.02), Tillering–Elongation (BA 0.70 ± 0.03 vs. global BA 0.64 ± 0.03), and Ripening (BA 0.66 ± 0.02 vs. global BA 0.56 ± 0.02). The global model was retained at Reproductive, where it outperformed the per-stage model (global BA 0.64 ± 0.03 vs. per-stage BA 0.59 ± 0.02). Figure 6b shows the independent test outcome. The training signal was corroborated at Early Vegetative and Ripening, where per-stage outperformed global, and at Reproductive where both remained near chance. At Tillering–Elongation, however, the global model generalized better on the independent test (BA 0.83 ± 0.01 vs. per-stage BA 0.78 ± 0.02), indicating that the per-stage cross-validation signal may be overfitted at this stage.

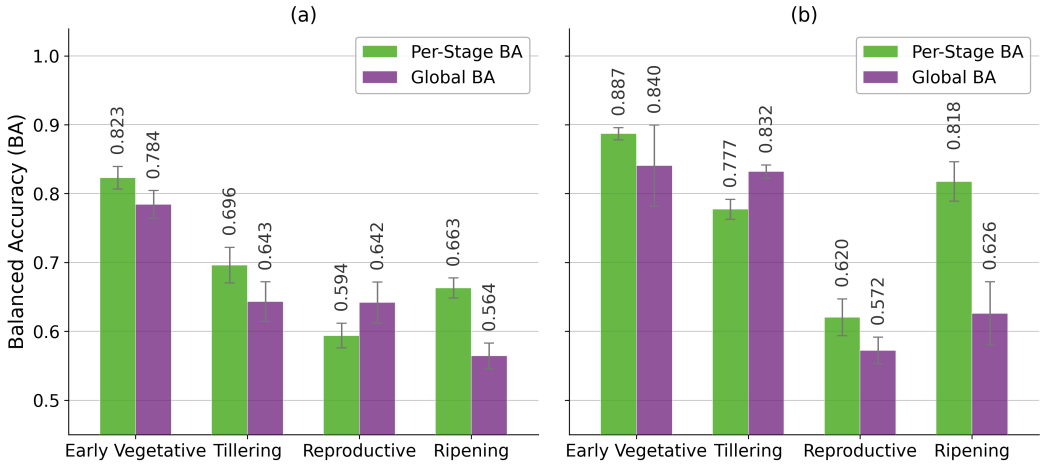


Figure 6. Per-stage routing evaluation across four rice growth stages (mean ± 1 SD across five stratified holdout sets). (**a**) Routing signal based on training data only. (**b**) Independent test outcome.

Table 5 reveals stage-specific recall and precision asymmetries. At Early Vegetative, Non-inundated recall was 1.00 ± 0.00 across all five holdout sets while Inundated recall was 0.77, indicating that 23% of flooded observations were systematically misclassified as Non-inundated. Non-inundated precision was 0.57, confirming a tendency to over-predict dry conditions at this stage. At Tillering–Elongation, the asymmetry reversed. Inundated recall (0.83) exceeded Non-inundated recall (0.73), consistent with canopy volume scattering during stem elongation suppressing the dry-soil backscatter signal. At Reproductive, Non-inundated recall (0.53) was near chance while Inundated recall (0.65) was moderately above

chance. At Ripening, recall was balanced (Non-inundated 0.84, Inundated 0.79) as canopy senescence partially restored the soil-water backscatter contrast. Stage-specific confusion matrices visualising the per-class recall patterns are provided in Figure S1.

Feature discrimination between Non-inundated and Inundated classes was characterized using model-independent Mann–Whitney U tests ($\Delta\bar{x}$: mean difference, Non-inundated minus Inundated; Cohen's d: standardised effect size) across the full combined dataset (Figure 7). Separability varied substantially across growth stages, peaking at Tillering–Elongation and declining sharply at Reproductive. At Early Vegetative (days 0–35), surface scattering ($\Delta\bar{x} = +4.25$ dB, $d = 0.75$, $p < 0.001$) and VV backscatter ($\Delta\bar{x} = +3.28$ dB, $d = 0.64$, $p < 0.001$) showed the largest class separation, consistent with L-band sensitivity to the soil-water contrast beneath a sparse canopy. At Tillering–Elongation (days 36–60), all six features were statistically significant ($p < 0.05$), with HV and volume scattering exhibiting the largest effect sizes, reflecting enhanced canopy–radar interaction during stem elongation. At Reproductive (days 61–90), surface scattering and double-bounce were no longer significant ($p > 0.05$) and overall feature separability diminished substantially, consistent with full canopy closure attenuating the soil-water contrast and explaining the near-chance classifier performance (BA = 0.59) at this stage. At Ripening (days 91+), HV and volume scattering remained discriminative as canopy senescence partially restored the soil-water backscatter contrast.

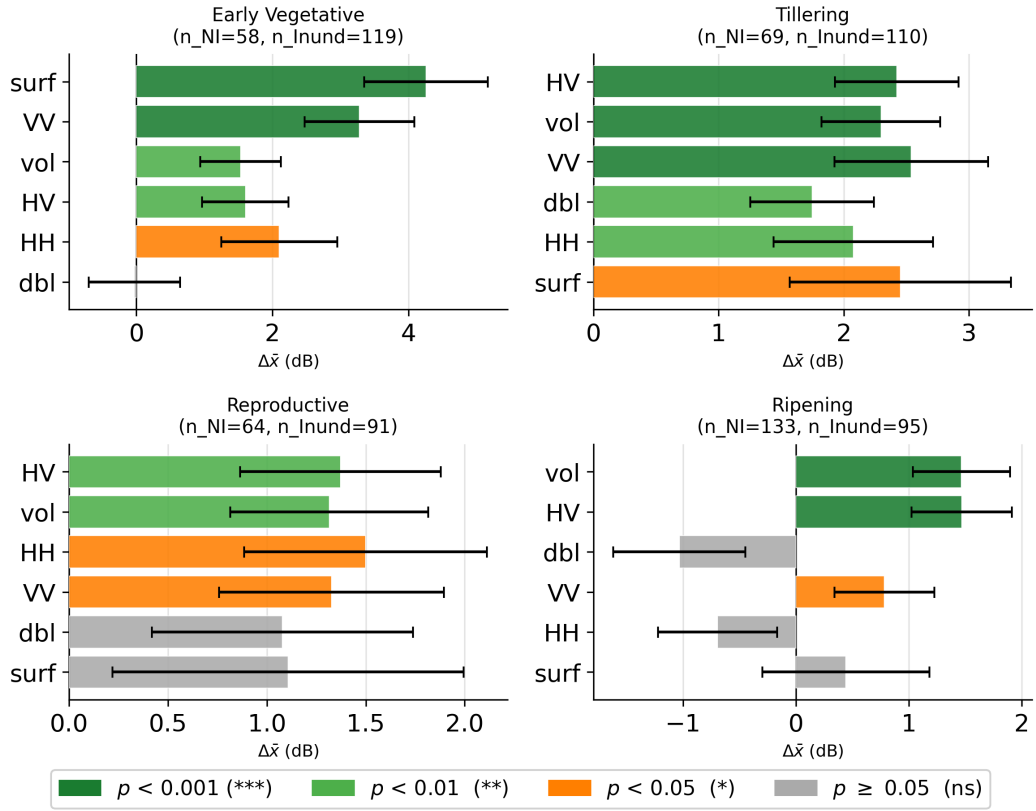


Figure 7. Model-independent feature–class separation per rice growth stage. Each bar shows the mean difference between classes ($\Delta\bar{x}$, Non-inundated − Inundated) based on Mann–Whitney U tests across the full combined dataset.

3.3. Rice Methane Emission Estimation

To isolate the contribution of each pipeline component to overall CH_4 estimation error, a four-track counterfactual decomposition was applied to the 20 holdout plots in each of the five sets. Phenology detection succeeded for 97 of 100 plot-season evaluations. The three missed detections were excluded from the CH_4 decomposition.

Table 6 summarizes the decomposition results against the mean ground-based CH_4 calculation of 86.7 ± 3.0 $kgCH_4\ ha^{-1}$. Phenology error was small and stable across sets (MAE_{pheno} = 5.9 ± 1.6 $kgCH_4\ ha^{-1}$, 6.8% mean error with range 3.8–7.6%). It showed a consistent negative bias (MBE_{pheno} = −2.9 ± 1.1 $kgCH_4\ ha^{-1}$) from the algorithm detecting slightly shorter growing seasons. Water level classification was the dominant error source ($MAE_{water\text{-}level}$ = 15.7 ± 5.1 $kgCH_4\ ha^{-1}$, 18.1% error with range 8.8–20.9%). It also had greater cross-set variability and a positive mean bias ($MBE_{water\text{-}level}$ = +6.6 ± 6.0 $kgCH_4\ ha^{-1}$) driven by SF overassignment in plots with brief or partial drainage events.

Table 6. CH_4 error decomposition summary (mean ± SD across five stratified holdout sets, 20 holdout plots each). $CH_{4\ pheno}$ detected duration with ground-truth SF (isolates phenology error); $CH_{4\ water\text{-}level}$ used ground-truth duration with SAR-based predicted SF (isolates water level error); $CH_{4\ full}$ applied both SAR-derived inputs (full pipeline).

	$CH_{4\ pheno}$	$CH_{4\ water\text{-}level}$	$CH_{4\ Full}$
MAE ($kgCH_4\ ha^{-1}$)	5.9 ± 1.6 (6.8%)	15.7 ± 5.1 (18.1%)	18.5 ± 4.5 (21.4%)
MBE ($kgCH_4\ ha^{-1}$)	−2.9 ± 1.1	+6.6 ± 6.0	+3.5 ± 5.8
SF match	—	58% ± 12%	58% ± 12%

The full pipeline produced MAE_{full} of 18.5 ± 4.5 $kgCH_4\ ha^{-1}$ (21.4% error) and MBE_{full} of +3.5 ± 5.8 $kgCH_4\ ha^{-1}$. The modest positive net bias arose from partial cancellation between the opposing phenology and water-level components described above. Across all detected plot evaluations, 46% fell within ±10% and 62% fell within ±20% of the ground-based CH_4 estimate. Figure 8a shows per-plot CH_4 estimate distributions across all four evaluation tracks, illustrating the spread attributable to each pipeline component. Figure 8b contextualizes algorithmic errors against the IPCC Tier 1 EF structural range at 0.83–1.81 $kgCH_4\ ha^{-1}\ day^{-1}$ or −32% to +48% of the default, which corresponds to −27.7 to +41.9 $kgCH_4\ ha^{-1}$ for the mean baseline. This structural error exceeds MAE_{full} by 1.5 to 2.3 times and MAE_{pheno} by 4.7 to 7.1 times, confirming that EF selection is the dominant uncertainty source for any Tier 1-based approach regardless of SAR algorithm performance.

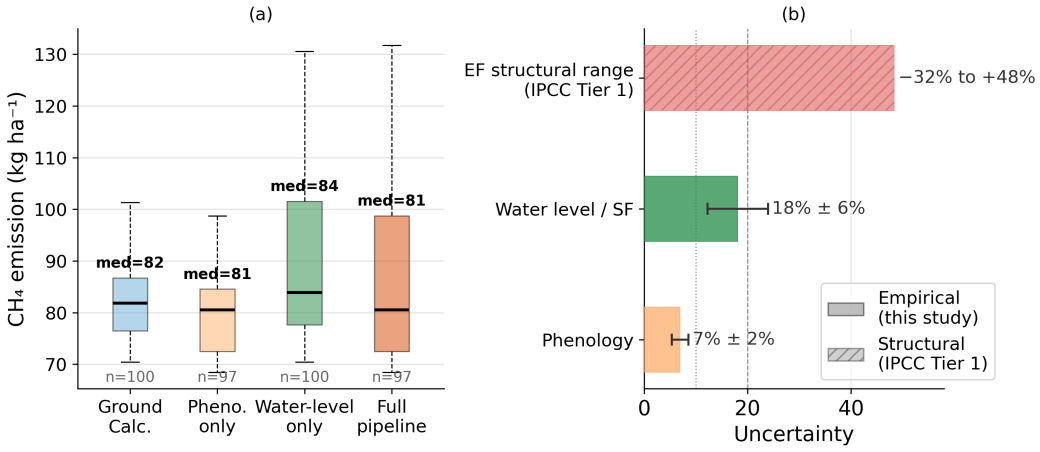


Figure 8. CH_4 estimation outcomes and uncertainty context. (**a**) Distribution of CH_4 estimates across all four evaluation tracks; (**b**) Uncertainty source hierarchy expressed as a percentage of the mean ground-based CH_4 calculation.

Figure 9 presents six representative cases selected to span the primary error modes of the decomposition, intended as failure-mode diagnostics rather than characterizations of typical behavior. Figure 9a,b show phenology-dominated errors, where residuals of 10–13 $kgCH_4\ ha^{-1}$ trace to 11–20-day duration underestimates from early planting

detection. Figure 9c–e illustrate water-level-dominated outcomes across both SF mismatch directions. The misclassifications that cross an SF class boundary produce errors of -64 to $+65$ $kgCH_4\ ha^{-1}$ regardless of overall classifier accuracy. Figure 9f demonstrates cross-pipeline compounding, where a modest phenology offset shifts the ALOS-2 evaluation window and excludes a genuine drainage event from the n_{dry} count, amplifying the water-level error to yield $\Delta_{full} = +75$ $kgCH_4\ ha^{-1}$ even though neither component fails in isolation. Figure 10 places these patterns in spatial context for a representative seven-plot cluster, illustrating how geographically proximate plots can yield markedly different SAR-derived water regime assignments and CH_4 estimates.

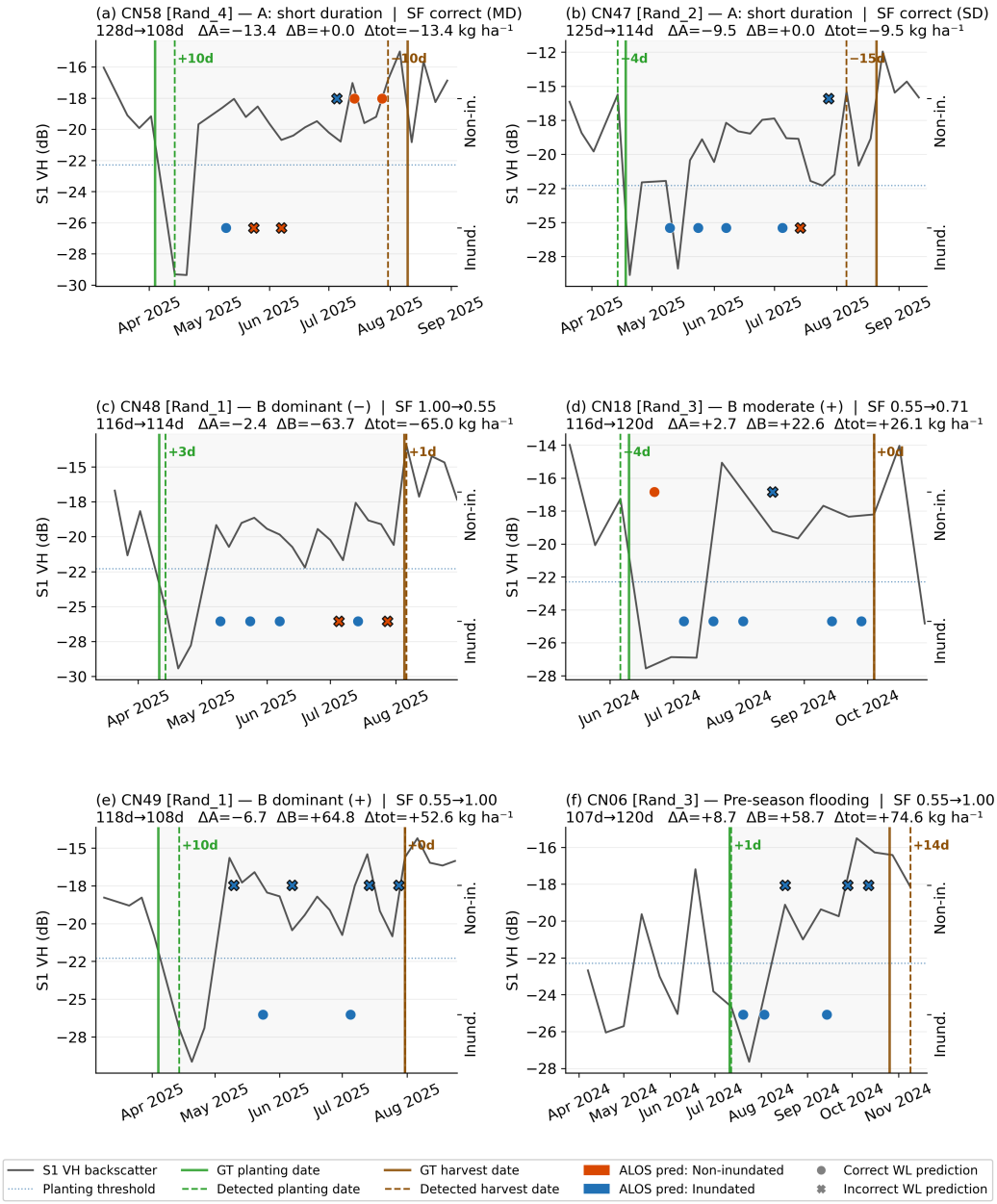


Figure 9. Six examples of CH_4 estimation outcomes with per-track error decomposition (Δ_{pheno}, $\Delta_{water\text{-}level}$, Δ_{full}, in $kgCH_4\ ha^{-1}$).

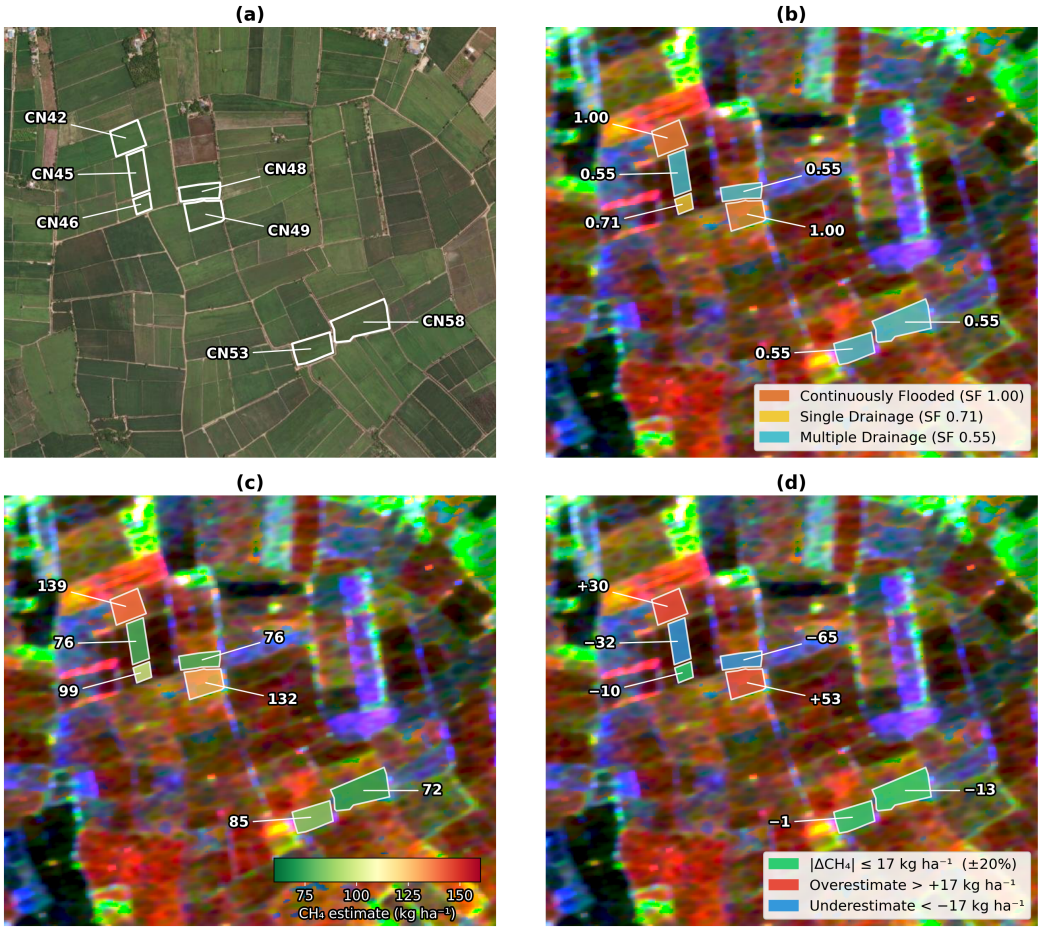


Figure 10. Spatial outputs for a representative seven-plot cluster (Set_1), displayed over ALOS-2 PALSAR-2 false-colour composite imagery (7 June 2025). (**a**) Field boundaries on satellite basemap with plot identifiers. (**b**) SAR-derived water regime class. (**c**) Full-pipeline CH_4 estimate (kg ha^{-1}). (**d**) Full-pipeline estimation error Δ_{full} (kg ha^{-1}).

4. Discussion

4.1. SAR Physics and Model Generalization

The multi-sensor design addresses a fundamental trade-off between C-band and L-band SAR for rice monitoring. C-band Sentinel-1 provides the temporal density needed to resolve phenological transitions. Its shorter wavelength, however, penetrates poorly beneath a rice canopy, limiting its utility for water level discrimination. L-band ALOS-2 penetrates the canopy to sense the soil-water surface. Its 14-day revisit interval is too sparse to characterise phenological timing reliably [21]. This study combines both sensors, using Sentinel-1-derived season boundaries to gate the ALOS-2 water level evaluation. The propagation of sensor-specific sampling uncertainty through to end-to-end CH_4 error has not previously been quantified.

The Sentinel-1 phenology detection performance is competitive with established benchmarks for Southeast Asian rice. Sentinel-1 VH-based algorithms typically report planting timing errors of 7–14 days in tropical lowland irrigated rice [16–18]. Phung et al. [32] reported planting and harvesting RMSE of 6.2 and 5.7 days for the Mekong Delta, comparable to the present study. The 97% operational detection rate supports automated deployment without manual quality control.

L-band inundation discrimination accuracy varies systematically with growth stage. During the Early Vegetative stage, sparse canopy allows the L-band signal to interact directly with the soil-water surface, yielding high classification accuracy. As the canopy

closes, accuracy degrades progressively, a pattern documented across multiple PALSAR and PALSAR-2 studies [9,21,25]. Segami et al. [25] quantified this as a decline in classification accuracy from 88% to approximately 62% once plant height exceeds 70 cm. Per-stage BA declined from 0.89 at Early Vegetative to 0.59 at Reproductive, corroborating this pattern. Arai et al. [30] reported an analogous decline in the Mekong Delta. At Reproductive, the per-stage model offers no cross-validation advantage over the global model. The routing, therefore, falls back to the global classifier as a direct response to this physical constraint.

The stage-dependent feature importance patterns are consistent with established L-band scattering models for flooded rice. At Early Vegetative, the soil-water surface return dominates the polarimetric signal through a sparse canopy. Freeman–Durden decomposition isolates this surface component more cleanly than raw polarimetric channels, removing the volume and double-bounce contributions mixed into VV and HH [20,27,33]. At Tillering–Elongation, stem-water double-bounce and volumetric scattering increase as the canopy develops. Multiple features contribute jointly to class separation at this stage [21,30]. At Reproductive, discriminability collapses across all six features. This is a saturation effect that polarimetric feature engineering alone cannot overcome [21,25].

4.2. End-to-End CH_4 Estimation

The ground-based CH_4 calculation (86.7 $kgCH_4\ ha^{-1}$) is an IPCC Tier 1 estimate driven by field-measured activity data and is not equivalent to a direct chamber flux measurement. Direct comparison with measured fluxes would require locally calibrated emission factors that account for soil carbon stocks, cultivar-specific methanogenesis rates, and organic amendment history, and is deferred to future work.

The full-pipeline MAE of 18.5 ± 4.5 $kgCH_4\ ha^{-1}$ (21.4%) is broadly comparable to prior satellite-based CH_4 estimation studies in Southeast Asian irrigated rice. Arai et al. [30] reported per-plot errors of 15–25 $kgCH_4\ ha^{-1}$ using ALOS-2 PALSAR-2 polarimetric decomposition in the Mekong Delta. Torbick et al. [13] reported regional-scale relative errors of approximately 15–30% using multi-sensor fusion in the Red River Delta. Beyond accuracy, the four-track error attribution distinguishes this framework from prior single-holdout designs. It directly identifies whether phenology or water-level estimation is the binding constraint on CH_4 accuracy, which aggregate error metrics alone cannot reveal.

The relative magnitude of phenology and water-level errors reflects the different temporal sampling regimes of the two sensors. The denser Sentinel-1 time series provides sufficient redundancy for the phenology algorithm to tolerate individual backscatter anomalies, yielding stable MAE_{pheno} across sets. With only 6 to 9 ALOS-2 acquisitions per season, individual acquisitions carry disproportionate weight in the SF assignment. A single misclassification can, therefore, shift the water-level class assignment. The four-track decomposition links this sensitivity to the 14-day ALOS-2 revisit interval, explaining the dominance of $MAE_{water\text{-}level}$ over MAE_{pheno}.

Figure 8b shows that the IPCC Tier 1 EF structural range (-32% to $+48\%$ of the default) overshadows both algorithmic error components by factors of 1.8 to 7.1. This identifies EF selection as the ceiling on absolute accuracy for any Tier 1-based approach. The default SF values carry analogous structural uncertainty of -25% to $+32\%$ per water regime [7]. Saunois et al. [2] identified rice as a major contributor to global methane budget uncertainty, driven by emission factor heterogeneity rather than activity data errors. These results establish that improving SAR algorithm accuracy has limited impact on absolute CH_4 estimation until EF and SF uncertainty is addressed.

The national inventory comparison supports the Tier 1 default at the regional scale. Estimated emissions converge within 2% for the Continuously Flooded wet season and within 1% for the single-drainage dry season [5,7]. Regional agreement does not, however,

preclude substantial per-plot deviations driven by local soil carbon stocks, cultivar-specific methanogenesis rates, and organic amendment history. Tier 2 estimation addresses this by replacing the default EF with locally calibrated rates. Ouyang et al. [10] found that field-constrained Tier 2 budgets across Monsoon Asia deviated from Tier 1 inventories by 20–40% at the regional level. The per-plot season duration and water regime classifications produced by this framework are precisely the activity data a Tier 2 calculation requires. Local EF calibration is, therefore, the highest-impact improvement pathway for future MRV applications.

4.3. Limitations and Future Work

The current framework has four primary limitations. First, the 14-day ALOS-2 revisit cycle creates a temporal gap in which short-duration drainage events occurring entirely between consecutive acquisitions go undetected. Spatial boundary effects from surrounding bunds and vegetation also necessitate a two-pixel interior buffer, which reduces the effective footprint of small plots. Future integration of more frequent L-band observations from ALOS-4, NISAR, and possibly ROSE-L will reduce the temporal gap and improve intra-season inundation tracking [34].

Second, the Continuously Flooded and Single Drainage water management classes remain underrepresented in the holdout evaluation. The mean SF match rate of 58% ± 12% across all sets, and the high variance in $MAE_{water\text{-}level}$ (range 8.8–20.9 $kgCH_4\ ha^{-1}$), partly reflect this class imbalance. Future work should prioritize balanced collection of Continuously Flooded and Single Drainage observations across multiple growing seasons to support statistically robust per-class accuracy assessment. In addition, a small number of experimental plots equipped with automated water-level loggers or subject to more frequent manual surveys would help characterise within-season water-level dynamics and improve understanding of how field conditions relate to SAR-derived classifications.

Third, canopy structure at the Reproductive and Ripening stages introduces an inherent classification blind spot. The Reproductive stage model operates near random classification, as full canopy closure at plant heights exceeding approximately 70 cm decouples SAR backscatter from the underlying surface water status [21,25]. This is particularly consequential for plots where mid-season drainage is practiced during Reproductive stage. Such events are simultaneously the most agronomically valuable to detect and the least likely to be correctly classified. The per-stage routing approach mitigates this by falling back to the global model at Reproductive where a per-stage model provides no improvement, but it does not resolve the underlying physical saturation. The practical consequence for CH_4 estimation is partly mitigated by common field management practice. AWD drainage targets the Tillering–Elongation stage and must be completed before panicle initiation. Drainage during the Reproductive period risks spikelet sterility and yield loss, and intentional drainage at this stage is, therefore, uncommon [8].

Fourth, the framework's applicability is presently restricted to irrigated lowland rice, covering both transplanted and broadcast-sown cultivation. The phenology detection algorithm exploits the sharp VH backscatter minimum that arises at field establishment (transplanting or broadcast seeding). Other rice systems may exhibit different water management practices and consequently different SAR temporal profiles. The five-set stratified holdout demonstrates within-system generalization across plots and growing seasons within this specific landscape, but does not substitute for cross-site or cross-system validation. Geographic extension to other irrigated rice landscapes in Southeast Asia would require, at minimum, a local parameter re-optimization and ground-truth data representative of the target system.

5. Conclusions

This study developed an automated multi-sensor SAR framework for estimating rice CH_4 emissions in irrigated paddies of the Central Plain of Thailand, evaluated across five stratified holdout sets (20 plots per set). The framework reliably detected growing seasons (97.0% ± 2.7%) and estimated planting and harvest dates to within 6–10 days on average. Water regime classification accuracy varied systematically by growth stage, from 0.89 at Early Vegetative to 0.59 at Reproductive, reflecting the physical limit of L-band canopy penetration at full canopy closure. A four-track counterfactual decomposition identified water-level classification as the dominant algorithmic uncertainty source ($MAE_{water\text{-}level}$ = 15.7 ± 5.1 kg CH_4 ha^{-1}, 18.1%), with phenology error remaining small and stable across sets (MAE_{pheno} = 5.9 ± 1.6 kg CH_4 ha^{-1}, 6.8%). The full pipeline produced MAE_{full} = 18.5 ± 4.5 kg CH_4 ha^{-1} (21.4%), yet both algorithmic errors were substantially smaller than the IPCC Tier 1 EF structural range (−32% to +48% of the default), establishing EF selection as the binding constraint on absolute CH_4 accuracy. The per-plot season duration and water regime classifications produced by this framework serve directly as IPCC activity data, supporting spatially explicit CH_4 estimation for national MRV systems. Priority improvement directions include more frequent L-band observations from ALOS-4, NISAR, and ROSE-L, and local EF calibration for Tier 2 estimation.

Supplementary Materials: The following supporting information can be downloaded at: https://www.mdpi.com/article/10.3390/rs18132194/s1, Table S1: Specifications of Sentinel-1 and ALOS-2 PALSAR-2 satellite data used in this study; Figure S1: Confusion matrices for each rice growth stage (Early Vegetative, Tillering–Elongation, Reproductive, Ripening) using the final routing model (per-stage SVM-RBF for Early Vegetative, Tillering–Elongation, and Ripening; global SVM-RBF for Reproductive). Values represent row-normalised recall from pooled test observations across five stratified holdout sets. Grand mean balanced accuracy: Early Vegetative 0.89 ± 0.01; Tillering–Elongation 0.78 ± 0.02; Reproductive 0.59 ± 0.01; Ripening 0.82 ± 0.03.

Author Contributions: Conceptualization, N.K., P.N. and T.L.T.; methodology, N.K., P.N., K.S. and T.L.T.; software, N.K. and K.S.; validation, N.K. and K.S.; formal analysis, N.K., P.N. and K.S.; investigation, N.K., P.N., K.S., K.K. and C.C.; resources, S.S.; data curation, N.K. and K.S.; writing—original draft preparation, N.K. and K.K.; writing—review and editing, N.K., P.N., K.K. and C.C.; visualization, N.K.; supervision, T.L.T.; project administration, K.K.; funding acquisition, K.K. All authors have read and agreed to the published version of the manuscript.

Funding: This research was supported by the National Science, Research and Innovation Fund (NSRF) and Thailand Science Research and Innovation (TSRI) [Grant Number: NRIIS 210226].

Data Availability Statement: The data that support the findings of this study are available from the corresponding author upon reasonable request.

Conflicts of Interest: Author Thuy Le Toan was employed by the company GlobEO. The remaining authors declare that the research was conducted in the absence of any commercial or financial relationships that could be construed as a potential conflict of interest.

References

1. IPCC. *Climate Change 2021: The Physical Science Basis. Contribution of Working Group I to the Sixth Assessment Report of the Intergovernmental Panel on Climate Change*; Cambridge University Press: Cambridge, UK, 2021. [CrossRef]
2. Saunois, M.; Stavert, A.R.; Poulter, B.; Bousquet, P.; Canadell, J.; Jackson, J.; Raymond, P.; Dlugokencky, E.; Houweling, S.; Patra, P.; et al. The Global Methane Budget 2000–2017. *Earth Syst. Sci. Data* **2020**, *12*, 1561–1623. [CrossRef]
3. Chen, Z.; Lin, H.; Balasus, N.; Hardy, A.; East, J.D.; Zhang, Y.; Runkle, B.R.K.; Hancock, S.E.; Taylor, C.A.; Du, X.; et al. Global Rice Paddy Inventory (GRPI): A High-Resolution Inventory of Methane Emissions from Rice Agriculture Based on Landsat Satellite Inundation Data. *Earth's Future* **2025**, *13*, e2024EF005479. [CrossRef]
4. FAO. *World Food and Agriculture—Statistical Yearbook 2023*; FAO: Rome, Italy, 2023. [CrossRef]

5. Thailand. *2024 Biennial Transparency Report (BTR)*; Technical Report; Ministry of Natural Resources and Environment: Bangkok, Thailand, 2024.
6. Butterbach-Bahl, K.; Sander, B.O.; Pelster, D.; Díaz-Piñes, E. Quantifying Greenhouse Gas Emissions from Managed and Natural Soils. In *Methods for Measuring Greenhouse Gas Balances and Evaluating Mitigation Options in Smallholder Agriculture*; Springer: Cham, Switzerland, 2016; pp. 71–96.
7. Buendia, E.; Tanabe, K.; Kranjc, A.; Jamsranjav, B.; Fukuda, M.; Ngarize, S.; Osako, A.; Pyrozhenko, Y.; Shermanau, P.; Federici, S. *2019 Refinement to the 2006 IPCC Guidelines for National Greenhouse Gas Inventories*; Technical Report; IPCC: Geneva, Switzerland, 2019.
8. Lampayan, R.M.; Rejesus, R.M.; Singleton, G.R.; Bouman, B.A. Adoption and economics of alternate wetting and drying water management for irrigated lowland rice. *Field Crops Res.* **2015**, *170*, 95–108. [CrossRef]
9. Bouvet, A.; Le Toan, T.; Lam-Dao, N. Monitoring of the Rice Cropping System in the Mekong Delta Using ENVISAT/ASAR Dual Polarization Data. *IEEE Trans. Geosci. Remote Sens.* **2009**, *47*, 517–526. [CrossRef]
10. Ouyang, Z.; Jackson, R.B.; McNicol, G.; Fluet-Chouinard, E.; Runkle, B.R.; Papale, D.; Knox, S.H.; Cooley, S.; Delwiche, K.B.; Feron, S.; et al. Paddy rice methane emissions across Monsoon Asia. *Remote Sens. Environ.* **2023**, *284*, 113335. [CrossRef]
11. Liang, R.; Zhang, Y.; Hu, Q.; Li, T.; Li, S.; Yuan, W.; Xu, J.; Zhao, Y.; Zhang, P.; Chen, W.; et al. Satellite-Based Monitoring of Methane Emissions from China's Rice Hub. *Environ. Sci. Technol.* **2024**, *58*, 23127–23137. [CrossRef] [PubMed]
12. Jang, J.; Kim, G.; Sim, J.; Kim, J.; Lee, Y. Machine Learning-Based Mapping of Daily Methane Concentration in Rice Paddies Using Meteorological Data and Satellite Images: A Case of South Korea. *Korean J. Remote Sens.* **2024**, *40*, 1095–1108. [CrossRef]
13. Torbick, N.; Salas, W.; Chowdhury, D.; Ingraham, P.; Trinh, M. Mapping rice greenhouse gas emissions in the Red River Delta, Vietnam. *Carbon Manag.* **2017**, *8*, 99–108. [CrossRef]
14. Arai, H.; Takeuchi, W.; Oyoshi, K.; Nguyen, L.D.; Inubushi, K. Estimation of methane emission from rice paddies in the Mekong Delta based on land surface dynamics characterised by ALOS-2 L-band SAR data. *Remote Sens.* **2018**, *10*, 1438. [CrossRef]
15. Rahmi, K.I.N.; Sofan, P.; Pratikasiwi, H.A.; Adriany, T.A.; Novresiandi, D.A.; Handika, R.; Arief, R.; Susilawati, H.L.; Rohaeni, W.R.; Cahyana, D.; et al. Utilization of Multisensor Satellite Data for Developing Spatial Distribution of Methane Emission on Rice Paddy Field in Subang, West Java. *Remote Sens.* **2025**, *17*, 2154. [CrossRef]
16. Clauss, K.; Ottinger, M.; Kuenzer, C. Mapping rice areas with Sentinel-1 time series and superpixel segmentation. *Int. J. Remote Sens.* **2018**, *39*, 1399–1420. [CrossRef]
17. Nguyen, D.B.; Gruber, A.; Wagner, W. Mapping rice extent and cropping scheme in the Mekong Delta using Sentinel-1A data. *Remote Sens. Lett.* **2016**, *7*, 1209–1218. [CrossRef]
18. Yang, H.; Pan, B.; Li, N.; Wang, W.; Zhang, J.; Zhang, X. A systematic method for spatio-temporal phenology estimation of paddy rice using time series Sentinel-1 images. *Remote Sens. Environ.* **2021**, *259*, 112394. [CrossRef]
19. Xu, S.; Zhu, X.; Chen, J.; Zhu, X.; Duan, M.; Qiu, B.; Wan, L.; Tan, X.; Xu, Y.N.; Cao, R. A Robust Index to Extract Paddy Fields in Cloudy Regions from SAR Time Series. *Remote Sens. Environ.* **2023**, *285*, 113374. [CrossRef]
20. Inoue, Y.; Kurosu, T.; Maeno, H.; Uratsuka, S.; Kozu, T.; Dabrowska-Zielinska, K.; Qi, J. Season-long daily measurements of multifrequency (Ka, Ku, X, C, and L) and full-polarization backscatter signatures over paddy rice field. *Remote Sens. Environ.* **2002**, *81*, 194–204. [CrossRef]
21. Hoshikawa, K.; Phontusang, P.; Katawatin, R. Synthetic aperture radar polarised backscattering behaviour in partially inundated agricultural fields. *Eur. J. Remote Sens.* **2023**, *56*, 2269305. [CrossRef]
22. Yagi, K.; Chairoj, P.; Tsuruta, H.; Cholitkul, W.; Minami, K. Methane emission from rice paddy fields in the central plain of Thailand. *Soil Sci. Plant Nutr.* **1994**, *40*, 29–37. [CrossRef]
23. Gorelick, N.; Hancher, M.; Dixon, M.; Ilyushchenko, S.; Thau, D.; Moore, R. Google Earth Engine: Planetary-scale geospatial analysis for everyone. *Remote Sens. Environ.* **2017**, *202*, 18–27. [CrossRef]
24. Phan, H.; Le Toan, T.; Bouvet, A. Understanding Dense Time Series of Sentinel-1 Backscatter from Rice Fields: Case Study in a Province of the Mekong Delta, Vietnam. *Remote Sens.* **2021**, *13*, 921. [CrossRef]
25. Segami, G.; Oyoshi, K.; Sobue, S.; Takeuchi, W. Characterizing L-Band Backscatter in Inundated and Non-Inundated Rice Paddies for Water Management Monitoring. *Remote Sens.* **2026**, *18*, 370. [CrossRef]
26. ESA. *Sentinel Application Platform (SNAP) v10*; European Space Agency: Paris, France, 2023.
27. Freeman, A.; Durden, S.L. A Three-Component Scattering Model for Polarimetric SAR Data. *IEEE Trans. Geosci. Remote Sens.* **1998**, *36*, 963–973. [CrossRef]
28. Meyer, H.; Reudenbach, C.; Hengl, T.; Katurji, M.; Nauss, T. Improving performance of spatio-temporal machine learning models using forward feature selection and target-oriented validation. *Environ. Model. Softw.* **2018**, *101*, 1–9. [CrossRef]
29. Cloude, S.R.; Pottier, E. A Review of Target Decomposition Theorems in Radar Polarimetry. *IEEE Trans. Geosci. Remote Sens.* **1996**, *34*, 498–518. [CrossRef]
30. Arai, H.; Takeuchi, W.; Oyoshi, K.; Nguyen, L.D.; Inubushi, K. Estimating the methane emission from rice paddies in the Mekong Delta through polarimetric analysis of ALOS-2 PALSAR-2 data. *Remote Sens. Environ.* **2022**, *274*, 112999. [CrossRef]

31. Amani, M.; Salehi, B.; Mahdavi, S.; Brisco, B. Separability Analysis of Wetlands in Canada Using Multi-Source SAR Data. *GISci. Remote Sens.* **2019**, *56*, 1233–1260. [CrossRef]
32. Phung, H.P.; Lam-Dao, N.; Nguyen-Huy, T.; Le-Toan, T.; Apan, A.A. Monitoring rice growth status in the Mekong Delta, Vietnam using multitemporal Sentinel-1 data. *J. Appl. Remote Sens.* **2020**, *14*, 014518. [CrossRef]
33. Huang, X.; Runkle, B.R.K.; Isbell, M.; Moreno-García, B.; McNairn, H.; Reba, M.L.; Torbick, N. Rice Inundation Assessment Using Polarimetric UAVSAR Data. *Earth Space Sci.* **2021**, *8*, e2020EA001554. [CrossRef] [PubMed]
34. Jones, C.E.; Rosenqvist, A.; Rommen, B.; Fitrzyk, M.; Rignot, E.; Scheuchl, B.; Zheng, Y.; Hooper, A.; Simons, M.; Kobayashi, T.; et al. Observation and Coordination Needs for Current, Near-Future, and Next Generation Earth-Observing SAR Systems. *Earth Space Sci.* **2026**, *13*, e2025EA004868. [CrossRef]

Disclaimer/Publisher's Note: The statements, opinions and data contained in all publications are solely those of the individual author(s) and contributor(s) and not of MDPI and/or the editor(s). MDPI and/or the editor(s) disclaim responsibility for any injury to people or property resulting from any ideas, methods, instructions or products referred to in the content.